

Experimental Investigation into Mechanisms for Energy Loss in a Rotating Magnetic Field Thruster

IEPC-2022-554

*Presented at the 37th International Electric Propulsion Conference
Massachusetts Institute of Technology, Cambridge, MA, USA
June 19-23, 2022*

Tate M. Gill¹, Christopher L. Sercel², and Benjamin A. Jorns³
University of Michigan, Plasmadynamics and Electric Propulsion Laboratory, Ann Arbor, MI, 48109

An investigation into the low thrust efficiency characteristic to rotating magnetic field (RMF) thrusters is presented. This work examines in detail the energy losses that occur during the initial plasma formation in these devices. Two energy loss mechanisms are evaluated: radiative losses due to excitation collisions, and wall losses due to thermal electron diffusion to the floating thruster walls. A triple Langmuir probe is used to make instantaneous measurements of the plasma density and electron temperature over the internal volume of a 5 kW-class rotating magnetic field thruster. The experiment is performed for six thruster operating conditions, where the mass flow rate, bias magnetic field strength, and RMF pulse length are varied. These results represent the first spatially and temporally resolved measurements of the internal plasma environment of these devices. It is found that radiative power dominates over power lost to the wall, as it contributes 80% of the total losses incurred during plasma formation and peaks instantaneously to powers of 300-500 kW. These radiative losses are found to be caused by high ion densities that reach values of $5 \times 10^{19} \text{ m}^{-3}$. Several techniques are proposed to mitigate these losses, including varying thruster geometry, switching to alternative propellants, and operating the thruster continuously.

I. Nomenclature

A	=	area
α	=	electron temperature dependent correction factor
β	=	probe potential dependent correction factor
E	=	energy
e	=	unit charge
ε	=	ion energy
ε^*	=	excitation energy
η	=	efficiency
f_{rep}	=	pulse repetition rate
I	=	electric current
J	=	impulse
j	=	current density
L	=	axial thruster length
M	=	integrated mass
\dot{m}	=	mass flow rate
m	=	particle mass
n	=	number density

¹Ph.D. Candidate, Department of Aerospace Engineering, University of Michigan, Ann Arbor, MI. AIAA Student Member

²Ph.D. Candidate, Department of Aerospace Engineering, University of Michigan, Ann Arbor, MI. AIAA Student Member

³Associate Professor, Department of Aerospace Engineering, University of Michigan, Ann Arbor, MI. AIAA Associate Fellow

P	=	power
ϕ	=	sheath potential drop
R	=	resistance
r	=	radial coordinate
r'	=	radial coordinate of thruster wall
$\langle\sigma^*\rangle$	=	mean excitation cross section
T_{eV}	=	electron temperature in eV
t	=	time
τ	=	time between pulses
Θ	=	characteristic divergence angle
V	=	voltage
\bar{v}_e	=	mean electron velocity
v	=	particle velocity
z	=	axial coordinate

II. Introduction

The most well-characterized electric propulsion (EP) technologies such as gridded ion thrusters (GIT) and Hall effect thrusters (HET) are well established in their ability to deliver high specific impulse propulsion and operate for missions lasting tens of thousands of hours. While well-proven, these devices exhibit several limitations. These include their power density, throttleability, and reliance on rare noble gasses for propellant. An alternative technology suited to address these limitations is a class of EP devices known as inductive pulsed plasma thrusters (IPPTs). Generally, IPPTs operate by sequentially discharging large primary coil currents to indirectly induce azimuthal mirror currents within the ionized plasma; these are then driven via the Lorentz force to produce thrust. Because the magnitude of both the plasma currents and the magnetic field scale with the driving coil current, the thrust scales quadratically with the achievable current density. Therefore, for a fixed current density, this magnetic acceleration mechanism allows the power output from IPPTs to scale like the device diameter to the fourth power as opposed to the quadratic scaling of electrostatic devices [1]. This becomes critical for developing high-power EP devices in the super-100 kW class. Additionally, since IPPTs operate in a pulsed mode, their thrust and time-averaged power consumption can be easily tailored to the given mission by changing only the pulse rate. In principle, this allows operation across a wide performance range while retaining a constant efficiency. Lastly, because the plasma currents are induced through the magnetic field, IPPTs do not require the use of plasma wetted electrodes, thus allowing them to be operated on propellants like water, CO₂, or ammonia, which can be derived from in-situ resource utilization [2].

Given these advantages, IPPTs have been the subject of several previous research works [3–6]. The most notable result of these efforts was the development of the Pulsed Inductive Thruster (PIT). The principle structure of the PIT consisted of a spiraling planar primary coil and a downstream neutral gas injector. In its most optimized configuration, the PIT exhibited 50% efficiency and 7000 s specific impulse operating on ammonia propellant [2, 7, 8]. However, the PIT suffered from two key challenges. Poor gas confinement due to the planar geometry inherently led to low mass utilization, and high voltages — up to 60 kV to drive the coil currents—posed both an arcing risk and major challenge for power processing.

The rotating magnetic field thruster (RMF) is an alternate IPPT technology, which is theorized to overcome the challenges associated with the PIT architecture. While sharing many of the advantages of traditional IPPTs, RMF thrusters use a different mechanism to drive the azimuthal plasma currents: they employ a series of transversely oriented antennas that discharge in series to form the eponymous rotating magnetic field. This field spins at a sufficiently high frequency to selectively entrain the electrons to form a circular current in the plasma that interacts with an applied magnetic field to drive the Lorentz force acceleration. Because the electron entrainment ideally only depends on the frequency of the RMF rather than the antenna current, there is an effective decoupling between antenna voltage and induced current. This in principle reduces the required voltage compared to the more typical PIT. Furthermore, the RMF antennas are arranged in a conical geometry, which increases the interaction time between the antennas and the neutral gas, thus improving mass utilization.

In light of these advantages, several groups have studied RMF thruster operation. Notable contributors include Magnetic Systems North West (MSNW) and the University of Washington, Tokyo University of Agriculture and Technology, and our work at the University of Michigan [9–14]. These studies have demonstrated that RMF thrusters, to

date, have exhibited poor efficiency. For example, MSNW indirectly inferred an 8% efficiency with a delivered impulse per shot of 1.0 mN-s for the ELF thruster [15]. More recently, we at the University of Michigan have operated our 5-kW class RMF thruster and directly measured (via a thrust stand) an per-shot impulse efficiency of 0.5% and 400 s specific impulse [16]. These results, which are underwhelming when compared to more mature concepts like Hall and ion thrusters, are puzzling in the context of theoretical predictions for RMF thruster performance. Indeed, it has been suggested that with an optimum RMF current drive efficiencies of up to 85% are theoretically achievable [9]. This invites the question as to what the major drivers for the efficiency loss in these devices are.

With this in mind, there have been several theories proposed to date to explain the low performance of RMF concepts. Both Polzin et al. [2] and Weber [15] state that large radiative losses, given the high densities in these devices, could compose a substantial energy sink. And, through their respective computational modeling work, Brackbill et al. [17] claimed that RMF thrusters are limited by low ionization-fraction and Koo et al. [18] showed that plasma instabilities can easily develop and hinder performance through increased resistivity. More recently, we performed measurements to characterize several phenomenological efficiency modes in RMF thrusters. In this work we showed that the majority of the energy coupled into the plasma is through thermal diffusion to the walls [19]. However, these results were limited in that they relied on single-point measurements of plasma properties. Indeed, close-to-centerline measurements were used to assess thermal flux, whereas there is strong numerical evidence to support the presence of substantial thermal gradients in the plasma [20]. As we discussed in our previous work, these types of two-dimensional features could impact our assessments of energy loss. The need is thus apparent to expand the spatial and temporal resolution of experimental measurements to assess the energy loss modes within an RMF thruster.

The goal of this work is to increase the resolution —both spatially and temporally— of probe-based measurements to understand the physics of the major energy loss mechanisms in RMF thrusters. To this end, this paper is organized in the following way. We begin in Sec. III with a review of both a phenomenological efficiency breakdown for RMF thrusters as well as the analytical framework we use to evaluate the theorized energy loss mechanisms and energy absorption from the RMF. We continue in Sec. IV with a description of the thruster test article, vacuum test facility, and plasma diagnostics employed. We then show in Sec. V our resulting measurements of the near-field plasma properties for several operational conditions and the evaluated energy loss mechanisms. Lastly, in Sec. VI we discuss the consequences of these results and frame them in context of future RMF thruster operation and design.

III. Phenomenological Efficiency Model

In this section, we review the operation and components of an RMF thruster, as well as our framework for analyzing their phenomenological efficiency modes. Furthermore, we define the equations we use to evaluate both the plasma power absorption from the RMF and the physical energy loss mechanisms we are interested in — namely thermal electron diffusion to the wall and radiative power loss due to electron ion excitation collisions.

A. Principles of Operation

We show in Fig. 1 a series of graphics which depict the fundamental operation of an RMF thruster. RMF thrusters operate in a pulsed mode, where plasma slugs are sequentially formed and then ejected from the thruster many times per second. A single pulse from an RMF thruster begins with a low-ionization-fraction seed plasma generated from a pre-ionization source filling the thruster volume which also contains a steady solenoidal magnetic bias field formed via a series of DC electromagnets. At this time, the primary RMF antennas — either two or more — are triggered in sequence with precisely controlled phase to form a transverse rotating magnetic field. The RMF entrains the electrons in the seed plasma and causes a cascading ionization of the remaining neutrals. The formed azimuthal electron current is subsequently magnetically accelerated from the thruster through a Lorentz interaction with the bias field and any formed self-field. The pulse concludes with the electrons exiting the thruster, carrying with them the heavier ions and providing impulse to the device. This process is repeated continuously to deliver quasi-steady-state thrust.

B. Phenomenological Efficiency Modes

Here, we introduce an expression for the efficiency of an RMF thruster as the product of several terms that represent individual contributions to overall efficiency. This discussion follows our previous work in Ref. [19]. We begin by defining overall efficiency in terms of the total impulse delivered per shot. This can be written as

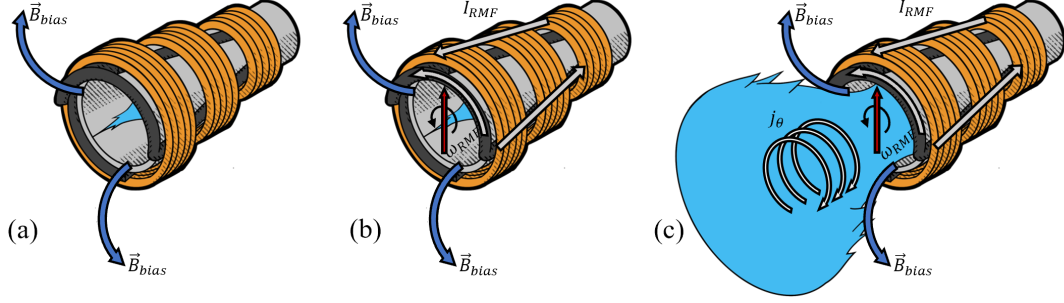


Fig. 1 RMF operational principles. (a) seed plasma fills thruster, which has a steady magnetic bias field, (b) RMF is formed via antennas, electrons are entrained, and ionization cascade begins, (c) large azimuthal electron current is formed and accelerated via the Lorentz force.

$$\eta = \frac{J^2}{2ME_{in}}, \quad (1)$$

where J is the impulse, M is the available propellant mass, and E_{in} is the input electrical energy. By decomposing this efficiency into a product of terms, we aim to quantify the various loss mechanisms inherent to RMF thrusters and provide a basis for the optimization of their operation. Following Gill et al. [19], we rewrite Eq. 1 into six components:

$$\eta = \eta_d \eta_m \eta_{pd} \eta_c \eta_p \eta_a, \quad (2)$$

- η_d is the divergence efficiency and is a measure of loss caused by radial ion velocity in the plume. This can be expressed as

$$\eta_d = \cos^2 \Theta, \quad (3)$$

where Θ is the characteristic divergence angle of the plume, which can be inferred from measurements of the current density in the far-field via Faraday probe.

- η_m is the mass utilization efficiency and represents how effectively the thruster ionizes propellant; it is written

$$\eta_m = \frac{M_i}{M}, \quad (4)$$

where M_i is the ejected ion mass for a single pulse, and M again is the available neutral propellant mass available for the shot.

- η_{pd} is a polydispersion correction for disparate ion velocities. This is expressed as

$$\eta_{pd} = \frac{\langle \sqrt{\varepsilon} \rangle^2}{\langle \varepsilon \rangle}, \quad (5)$$

where $\langle \sqrt{\varepsilon} \rangle$ is the average of the square root of ion energy which is proportional to ion velocity and $\langle \varepsilon \rangle$ is directly the average of ion energy.

- η_c is the coupling efficiency and represents how much of the input energy is coupled into the plasma. This is written as

$$\eta_c = \frac{E_p}{E_{in}}, \quad (6)$$

where E_p is the energy absorbed by the plasma and has constituent terms including the useful thermal and magnetic energies, but also ionization cost, wall losses, and radiative losses.

- η_p is the plasma efficiency and is characteristic of the energy in the plasma being stored in useful thermal and inductive modes. This is expressed as

$$\eta_p = \frac{E_B + E_{th}}{E_p}, \quad (7)$$

where E_B and E_{th} are the stored useful magnetic and thermal energy in the plasma respectively.

- η_a is the acceleration efficiency and reports how much of that thermal and inductive energy is successfully transferred to directed kinetic energy.

$$\eta_a = \frac{E_i}{E_B + E_{th}}, \quad (8)$$

where E_i is the total kinetic energy of the ions downstream after they have been accelerated by the RMF.

With these terms defined, we have a framework for interpreting the efficiency losses incurred by the RMF thruster. Previous work by Gill et al. [19] showed that three of these efficiency modes contributed to the majority of the performance loss for RMF thrusters. For the operation conditions investigated, divergence efficiency and coupling efficiency both contributed a factor between 30% and 40% to overall thruster efficiency, and most significantly, plasma efficiency was roughly 10%— or restated, a 90% energy loss. Given that the majority of input energy is lost during the plasma formation process, we would like to better understand the power flow within the system. In the following, we turn to the evaluation of two of the dominant power loss mechanisms.

C. Plasma Energy Balance

Here, we provide the basis for our calculations of absorbed plasma energy and the dominant loss mechanisms we seek to characterize — thermal electron diffusion to the walls and radiative power from excitation collisions. To evaluate the energy coupled to the plasma from the RMF, we make a measurement of the effective resistance of both the unloaded and plasma-loaded RMF circuit. This effective resistance is found by comparing the DC power input to an I^2R energy consumption per shot and is written as:

$$R_{eff} = \frac{I_{PS}V_{PS}}{\left(\int_0^\tau I_x^2 dt + \int_0^\tau I_y^2 dt\right) f_{rep}}, \quad (9)$$

where I_{PS} and V_{PS} are the DC current and voltage from the power supply, respectively, I_x and I_y are the currents through the 'x' and 'y' RMF antenna, f_{rep} is the pulse repetition rate, and $\tau = 1/f_{rep}$ is the pulse period. The notional circuit diagram for Eq. 9 is shown in Fig. 3(b), where we assume each antenna contributes half of the effective resistance to the PPU and that, while loaded, the plasma adds equally to these resistances. Additionally, we show a reference waveform for I_x in Fig. 3(a).

To calculate the energy input into the plasma we take the ratio of effective plasma resistance to the total loaded circuit resistance and multiply it by the energy consumed per shot, written as:

$$E_p = \frac{R_{loaded} - R_{unloaded}}{R_{loaded}} \frac{I_{PS}V_{PS}}{f_{rep}}, \quad (10)$$

where the effective plasma resistance is the difference between the loaded and unloaded circuit resistances $R_{plasma} = R_{loaded} - R_{unloaded}$.

The input plasma energy from Eq. 10 can be stored and lost through a number of channels. Primarily, we are concerned with the stored inductive and thermal energy, ionization cost, thermal flux to the walls, and radiative power due to collisions. From our previous work, we found that the energy in the useful modes — inductive and thermal — is effectively converted into kinetic energy downstream and that ionization energy is a relatively small cost relative to the other losses [19]. Therefore, the focus of this work is to evaluate the remaining two identified loss modes — wall flux and radiative power.

Following the description by Goebel and Katz [21], we take the electron power flux to the walls per unit area as

$$P_{wall} = \frac{1}{4} ne \sqrt{\frac{8eT_{eV}}{\pi m_e}} (2T_{eV} + \phi) \exp\left(\frac{-\phi}{T_{eV}}\right), \quad (11)$$

where n is the plasma density, T_{eV} is the electron temperature in eV, ϕ is the potential drop across the sheath, which for our floating walls we take as the floating voltage for a Maxwellian plasma:

$$\phi = T_e v \sqrt{\frac{2m_i}{\pi m_e}}, \quad (12)$$

where m_i and m_e are the ion and electron masses, respectively. To calculate the energy lost from this electron flux over a pulse, we integrate the electron power over the inner thruster wall area and over the duration of the pulse. The wall loss energy is then,

$$E_{wall} = \int_0^\tau \left(\int_0^L 2\pi r'(z) P_{wall} dz \right) dt, \quad (13)$$

where again τ is the time between pulses, L is the thruster length, and $r'(z)$ is the radial coordinate of the wall at axial position z .

Furthermore, we calculate the collisionally driven radiated power per unit volume using the following equation:

$$P_{rad} = n^2 \langle \sigma^* \rangle \bar{v}_e \varepsilon^*, \quad (14)$$

where again n is the plasma density, $\langle \sigma^* \rangle$ is the mean excitation cross-section, \bar{v}_e is the mean electron velocity, and ε^* is the energy released per excitation collision. We use the numerical fit for the mean excitation cross-section as a function of electron temperature provided by Mikellides et al. [22], and the constant value for excitation energy, $\varepsilon^* = 8.32$ eV from Hayashi et al. [23, 24]. In a similar manner to the integrated wall loss energy, we write the total radiated energy over a pulse as:

$$E_{rad} = \int_0^\tau \left(\int_0^L \int_0^{r'(z)} 2\pi P_{rad} r dr dz \right) dt, \quad (15)$$

where, τ is the pulse period, L is the thruster length, and $r'(z)$ is the radial coordinate of the wall at axial position z .

It is worth noting here the dependence on density for the two loss terms in Eqs. 11 and 14. The thermal wall losses scale linearly with plasma density; however, radiative losses scale quadratically with plasma density. Furthermore, these two losses can be calculated solely from measurements of the plasma density and electron temperature. Therefore, the primary focus of our experiment was to measure these plasma properties during RMF thruster operation.

IV. Experimental Setup

In this section, we describe the experimental setup for this work. This includes overviews of the test article, the measurement diagnostics employed, and the test facility.

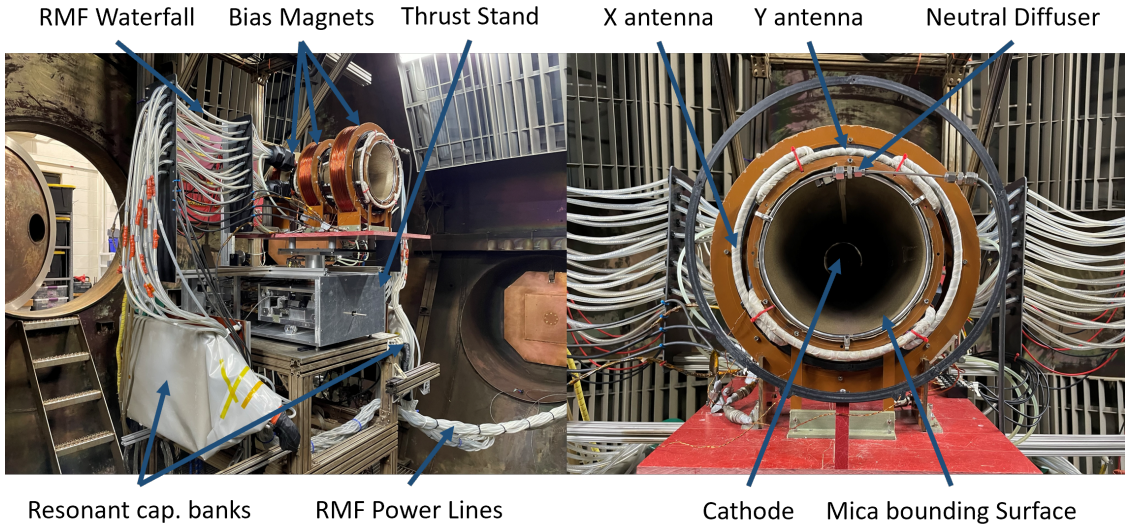


Fig. 2 Labeled diagram of major thruster components

A. Test Article and Power Supply

For this experiment, we performed measurements of the plasma properties of the PEPL RMFv2 Thruster. We show in Fig. 2 the test article inside the Large Vacuum Test Facility at the University of Michigan with the major subsystem components labeled. The thruster consists of five major components. The RMF is produced by a pair of orthogonally oriented saddle coils which are fired electrically 90 degrees out of phase. In Fig. 3(a) we show an example discharge waveform from the 'x' antenna during plasma loaded operation. The currents in these coils are driven by a 4 kW resonant switching power supply developed by Eagle Harbor technologies [25]. This power processing unit converts high voltage DC power to high-frequency pulsed AC by driving an LC circuit at its resonant frequency. In Fig. 3(b) we show a simplified schematic of the RMF circuitry with relevant elements labeled. We provide a seed plasma to the thruster cone using a 20 A LaB6 hollow cathode, which discharges to an annular steel anode. We use a set of three DC bias magnets to supply the magnetic field for the applied field component of the Lorentz force acceleration; the field is shaped such that the field lines follow the inner wall of the thruster. The structure of these magnets — as well as the rest of the thruster, where possible — is constructed from non-conductive fiberglass to minimize eddy-current losses [14]. We use an annular neutral injector located at the exit plane of the thruster to source the majority of our neutral propellant. The injector points upstream to increase the residency time of the gas. Finally, the thruster inner wall is fabricated from a flexible mica sheet that acts as a dielectric surface to bound the plasma. The influence of dimensional scaling and construction of the PEPL RMFv2 thruster is discussed further by Sercel et al. [16].

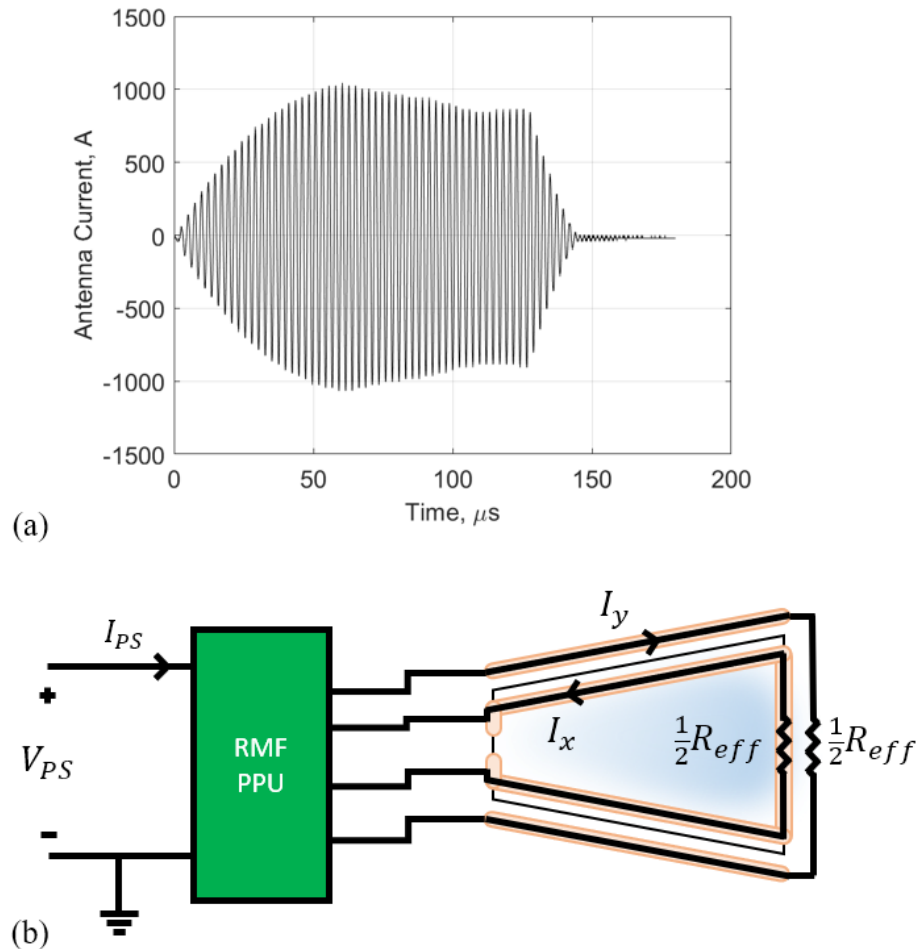


Fig. 3 (a) Discharge current waveform for 'x' antenna over one RMF pulse for operating condition 'b' in Table. 1. (b) RMF circuit schematic for energy coupling calculations.

We performed our measurement with six different thruster operating conditions, shown in Table 1. The methodology for these conditions was to start with a baseline case and vary the magnetic field strength, pulse duration, and the total

mass flow rate independently. The flow rates were chosen from optimum conditions identified during prior performance testing [16]. Compared to 120 G, however, we chose to increase the magnetic field strength, in an attempt to increase the confinement of the plasma and reduce wall losses, which have been previously theorized to be a primary loss mechanism [19]. The pulse length was also shortened to maximize coupling, as we theorized — due to the shape of the RMF antenna currents — that energy could be wasted after 125 μs [19].

Table 1 RMF thruster operating conditions for internal probing

Operating Parameter	Value					
Condition	a	b	c	d	e	f
Total Flow Rate [mg/s Xe]	4.0			5.4		
Peak Bias Magnetic Field [G]	120	180		120	180	
Pulse Length [μs]	125		200	125		200
Cathode Flow Rate [mg/s Xe]	1.3					
RMF Magnitude [kA pk-pk]	2.0					
Pulse Repetition Rate [Hz]	25					

B. Diagnostics

To measure the density and electron temperature — the plasma properties of interest as discussed in section III — we employ the use of a triple Langmuir probe (TLP), which we show in Fig.4(a). The TLP consists of three 0.127 mm diameter by 1.270 mm long thoriated tungsten wires oriented along the flow direction with 2 mm spacing. The TLP was operated consistent with Chen and Sekiguchi [26]; however, we use a 50:1 high voltage differential probe and 10 wraps around a 1 V/A Pearson coil for the voltage and current measurements, respectively, and the biased probes were at 28.8 V with respect to each other. We took measurements of 25 RMF pulses at each of 47 spatial locations and recorded the output voltage and current with a 16 bit digital oscilloscope capturing 1 MS/s. We then averaged over the 25 pulses for each physical measurement location to reduce error. Additionally, we placed two Pearson coils around the power lines for the RMF to obtain antenna discharge current waveforms to evaluate energy coupling per Eq. 10. These Pearson coils each had a sensitivity of 0.1 V/A, and we fed the output of the coils into 100:1 compensated oscilloscope probes and recorded at 80 MS/s.

C. Triple Langmuir Probe Operation

Triple Langmuir probes provide an instantaneous measurement of both electron temperature and density by effectively taking three points on the full plasma I-V curve, and rely on a Maxwellian plasma assumption. A typical TLP implementation, which we use here, can be seen in Figure 5. The probe consists of three electrodes, each at a different potential. We allow probe 2 to electrically float, and we enforce a floating bias voltage between probes 1 and 3, denoted V_{d3} . Using Kirchhoff's current law and the Boltzmann relation for electron current, we can form an equation for the current to each probe as a function of its voltage as:

$$I_1 = I_{i1} - A_p j_e \exp\left(\frac{V_1}{T_{eV}}\right) = -I \quad (16)$$

$$I_2 = I_{i2} - A_p j_e \exp\left(\frac{V_2}{T_{eV}}\right) = 0 \quad (17)$$

$$I_3 = I_{i3} - A_p j_e \exp\left(\frac{V_3}{T_{eV}}\right) = I, \quad (18)$$

where I_i is the ion current to each probe, A_p is the probe area, j_e is the electron saturation current density, $j_e = en\sqrt{eT_{eV}/2\pi m_e}$, and V is the potential of each probe. Following the derivation of [26], which assumes the ion current contributions to all the probes are equal, we can form an implicit relation between the measured differential voltage $V_{d2} = V_1 - V_2$ and the electron temperature. This is expressed as:

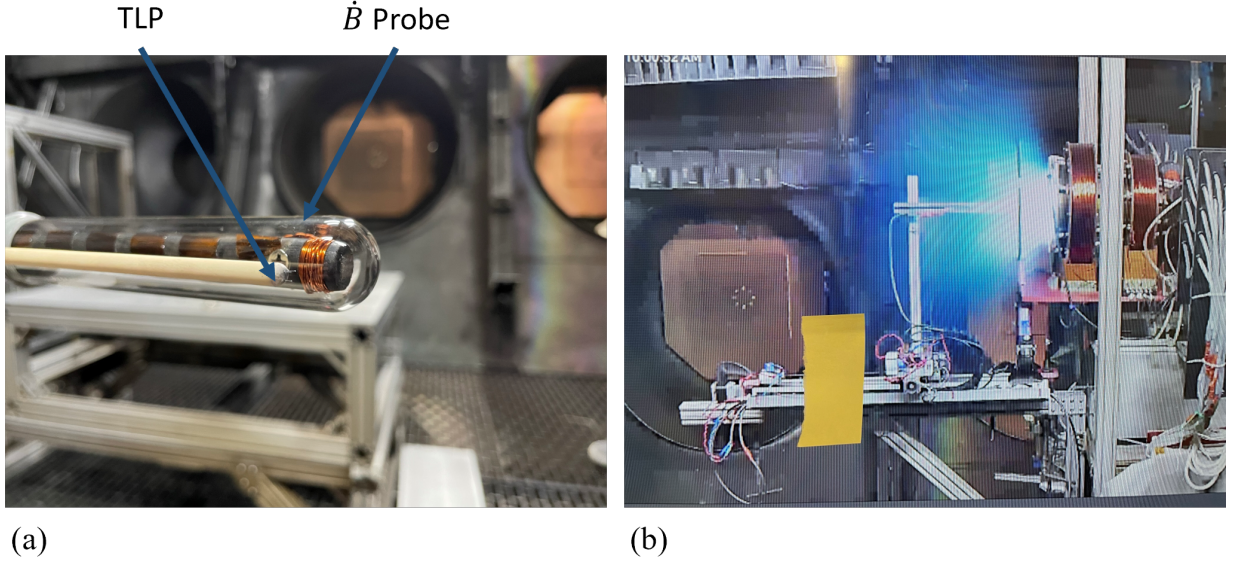


Fig. 4 a) Close up image of the triple Langmuir probe, and b) image of the motion stages injecting probes into thruster during operation.

$$\frac{1 - \exp(-V_{d2}/T_{eV})}{1 - \exp(-V_{d3}/T_{eV})} = 1/2. \quad (19)$$

This equation is presented graphically in Fig. 5(b).

To calculate the plasma density as measured by the TLP, we start by eliminating the shared term $A_p j_e$ from Eqs. 17 and 18 to arrive at an expression for the current carried by probes 1 and 3,

$$I = I_{i3}(V_3) - I_{i2}(V_2) \exp\left(\frac{V_{d2} - V_{d3}}{T_{eV}}\right), \quad (20)$$

where we now express the ion current contribution as a function of probe voltage (i.e. $I_{i3} = I_{i3}(V_3)$) because the losses we are interested in are more sensitive to density than electron temperature. For most Langmuir probe ion sheath models, the contribution of ion current can be expressed as the product of density, a electron temperature dependent factor, and a probe voltage dependant factor. We write this as:

$$I_i(V) = n\alpha(T_{eV})\beta(V). \quad (21)$$

Substituting this into Eq. 20, we can form the following expression for density,

$$n = \frac{I}{\alpha(T_{eV})} \left[\beta(V_3) - \beta(V_2) \exp\left(\frac{V_{d2} - V_{d3}}{T_{eV}}\right) \right]^{-1}. \quad (22)$$

Based on the geometry of the probe and the densities we expect from prior measurements [19], we will use orbital motion-limited (OML) theory for the expansion of the ion sheath [27]. In our framework, this is written as:

$$\alpha_{OML} = \frac{eA_p}{\pi} \quad (23)$$

$$\beta_{OML}(V) = \sqrt{\frac{2e(-V)}{m_i}}. \quad (24)$$

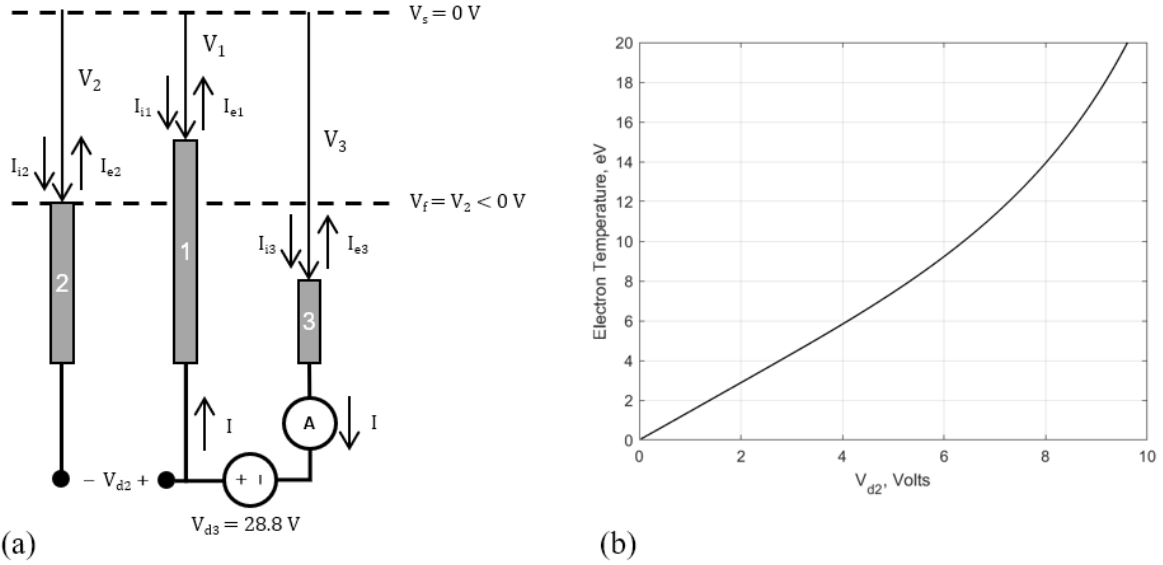


Fig. 5 (a) circuit diagram of TLP operation. (b) Function of measured voltage V_{d2} to electron temperature as described by Eq. 19.

D. Test facility and configuration

We performed our experimental campaign in the Large Vacuum Test Facility (LVTF) at the University of Michigan. This vacuum facility measures 6 m in diameter by 9 m long and can pump a maximum of 600 kL/s of xenon. However, for this experiment we utilized only 6 cryogenic pumps and the pressure inside the vacuum facility was monitored by a Stabil ion gauge aligned with the thruster exit plane and located 1 m radially from the thruster body. Background pressure during testing was on the order of 2.8×10^{-6} Torr Xe for the 4.0 mg/s flow condition and 3.7×10^{-6} Torr Xe for the 5.4 mg/s flow condition. Fig. 6 shows a schematic of the RMF thruster and associated diagnostics inside LVTF.

The TLP was mounted on a set of motion stages and swept in an axial and radial grid with 2 cm spacing from thruster centerline to the wall. Typically we allow the thruster body and cathode discharge to float electrically relative to chamber ground for our experimental measurements. However, for this study, a electrical short developed and the anode was at chamber potential. We believe this to be a minor impact to our measurements, as the RMF output is also floating and the thrust mechanism is ultimately electromagnetic and not electrostatic in nature.

V. Results

In this section we present the results from the TLP measurements taken in this work. We start by showing an example measurement from the TLP, and following this, we show a select number of the plasma properties in the RMF pulse for condition 'b' of Tab. 1 as a function of axial distance, radial distance and time. We then report the time-resolved spatially averaged density and electron temperature for all six of our operating conditions. Lastly, we show the associated calculations for both thermal wall losses and radiative power loss.

A. Raw TLP Data

We show in Fig. 7 a example raw trace from the TLP. Here, V_{d2} is the differential measured voltage between probes 1 and 2, and I is the current that passes through probes 1 and 3 as shown in Fig. 5(a). From the plot in Fig. 7, we can see that between 200 and 250 μs the measured voltage V_{d2} is negative. According to Fig. 5 and Eq. 19 this is non-physical and is likely the result of the probe becoming improperly biased once the plasma rarefies and ejects out of the thruster. Because we consistently see this effect in our measurements, we only present data for the first 200 μs after the onset of the RMF. We can justify this by quickly looking at Fig. 11 where the loss mechanisms we seek to characterize tend towards zero before our 200 μs cutoff. We discuss this consideration further in Sec. VI.

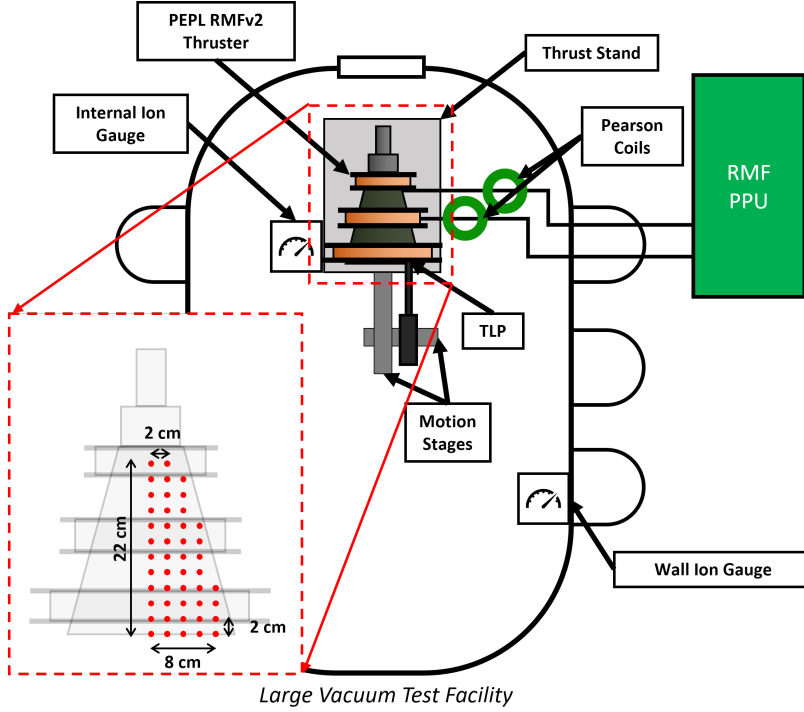


Fig. 6 Experimental setup inside the Large Vacuum Test Facility

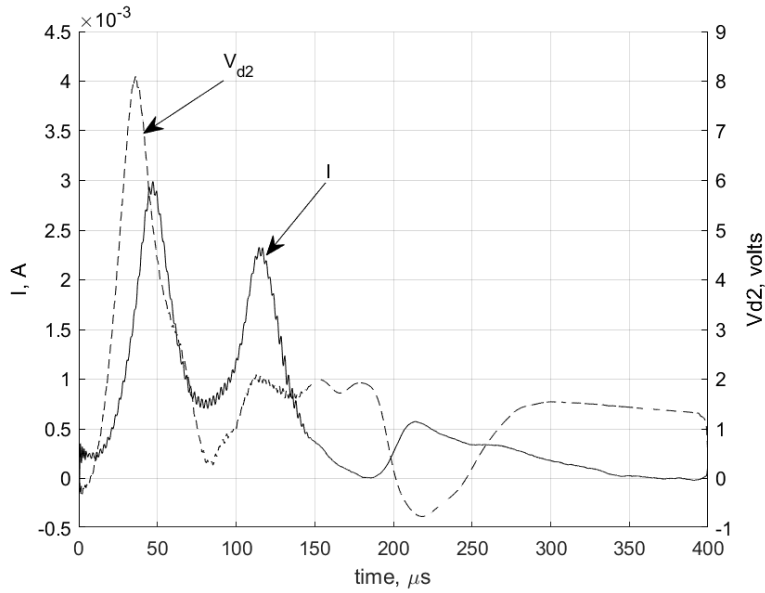


Fig. 7 Example raw TLP trace for V_{d2} and I

B. Internal Plasma Properties

Turning now to our measurements of plasma properties, we show in Fig. 8 the spatially resolved plasma density and electron temperature for several times during thruster operation at condition 'b' from Table 1, which is 4.0 mg/s total Xe flow, 120 G peak bias field strength, and 125 μ s pulse length. These results were calculated via Eqs. 19 and 22 using the instantaneous voltage and current V_{d2} and I measured by the TLP.

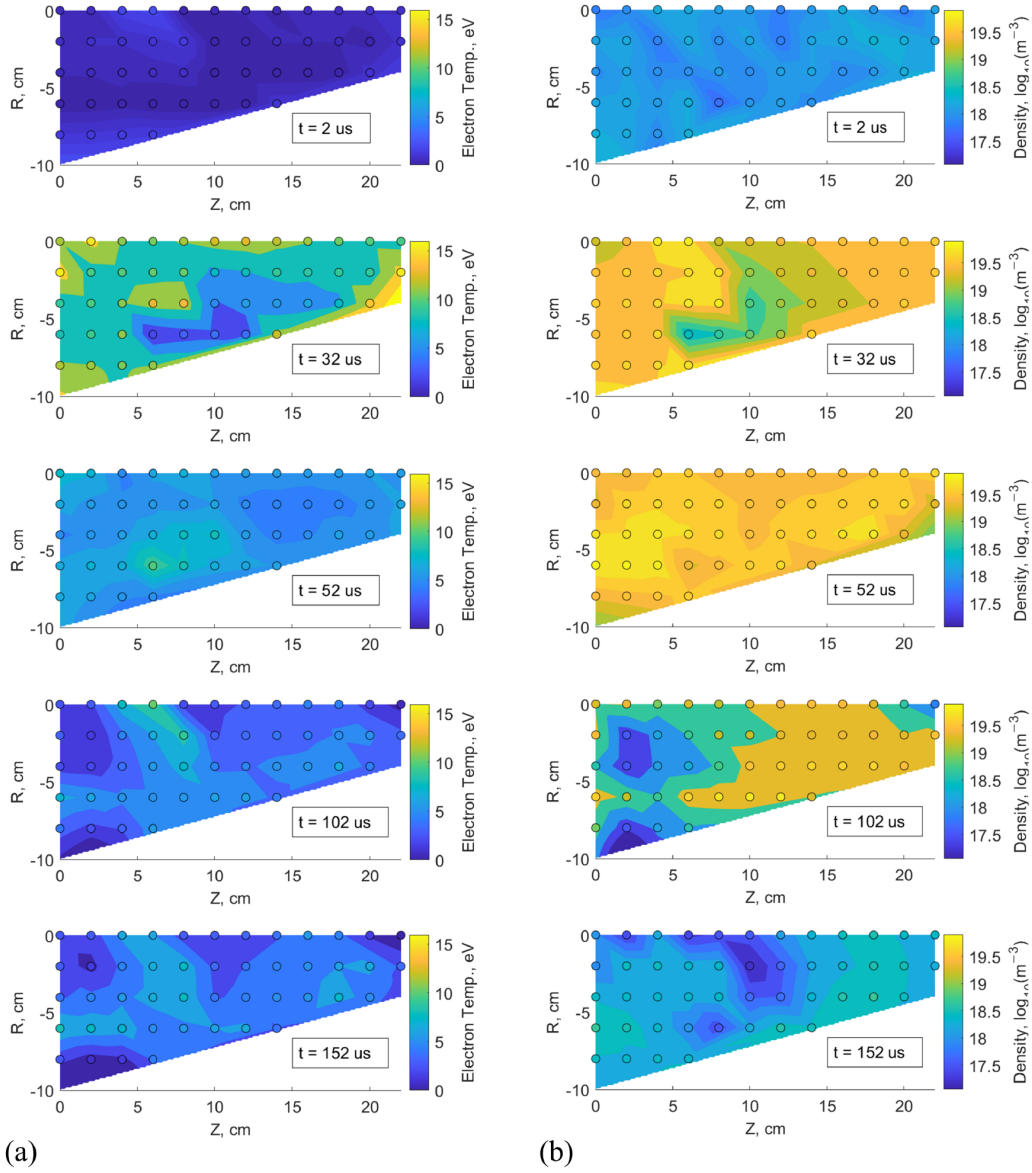


Fig. 8 Spatially resolved plasma properties for operating condition 'b' from Table.1. (a) Electron temperature in eV (b) Plasma density in $\log_{10}(\text{m}^{-3})$. The origin is located at the centerpoint of the thruster exit plane with the thruster pointing left.

From Fig. 8 we can see that for the electron temperature the peak is reached around $32 \mu\text{s}$ with most of the hot electrons (around 12-15 eV) formed near the back of the thruster near the wall. This follows intuition, as that is the location where the RMF fields are the strongest and the least uniform due to the close proximity to the RMF antennas. It further follows that non-uniform fields would cause more randomized motion of the electrons and thus increased heating. For plasma density, we see that the peak values occur at $52 \mu\text{s}$ which is notably after the electron temperatures peak. This is unsurprising given that the RMF ionization source couples energy into the free electrons which subsequently results in an ionization cascade. Furthermore, we note that during this maximum there is little spatial variation in the plasma density with the entire thruster volume reaching between $1\text{e}19 \text{ m}^{-3}$ and $1\text{e}20 \text{ m}^{-3}$. However, we do see that the maximum densities do occur off center-line which is consistent with field-reversed-configuration (FRC) plasmoids [20]. While interesting to note, the formation of FRCs is not an explicit target for our thruster, and the physics of these plasma structures is beyond the scope of this work.

We now show in Fig. 9 and Fig. 10 the spatial average of plasma density and electron temperatures for the operating conditions at 4.0 mg/s Xe flow and 5.4 mg/s Xe flow respectively. We calculated these values by taking the mean of all 47 spatial measurements (as shown in Fig. 8) at each sample time. We represent the spatial variance of the measurements with the overlaid filled areas in the figures. Across operating conditions, we can see that plasma density is generally formed by a Gaussian with with a peak on the order of $4 \times 10^{19} \text{ m}^{-3}$ occurring at around $50 \mu\text{s}$ for the 4.0 mg/s conditions and slightly earlier around $40 \mu\text{s}$ for the 5.4 mg/s conditions. It is interesting to note that there is also present a second peak for all cases occurring around $100 \mu\text{s}$, and furthermore, the higher flow rate does not result in a higher initial peak, but a higher secondary peak. This is perhaps an indication that there is a limit to the initial ionization and coupling and additional neutral particles are only utilized in subsequent pulses, however this is discussed further in Sec. VI. Turning now to the plots of electron temperature, we see that there is a similar initial Gaussian peak with electron temperatures reaching on the order of 10 eV. These electron temperatures peak and correspondingly earlier times than the plasma densities, as we noted previously for the spatially resolved plasma properties. As opposed to the densities, which quickly return a small background value, the electron temperatures remain above the background for a several hundred μs after the RMF pulses end.

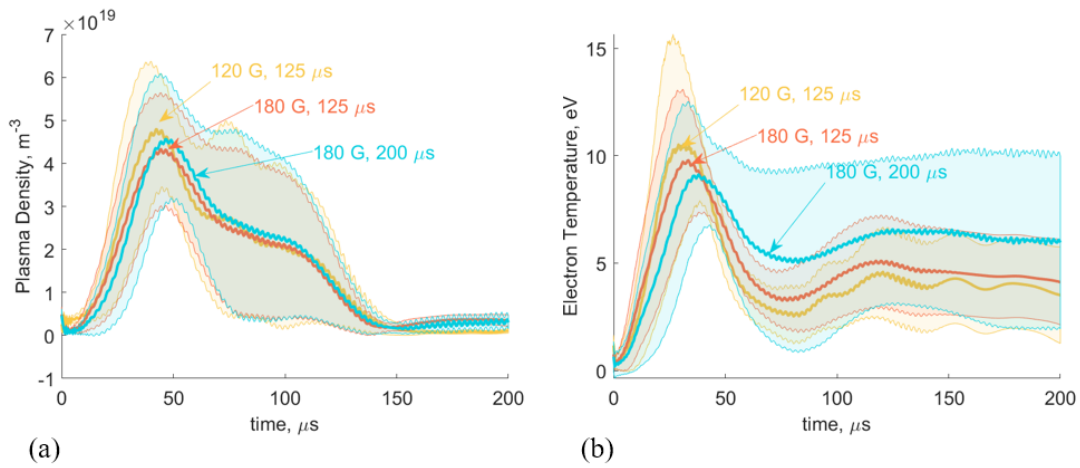


Fig. 9 Plots showing the a) plasma density and b) electron temperature for the 4.0 mg/s Xe flow rate conditions a-c in Table1

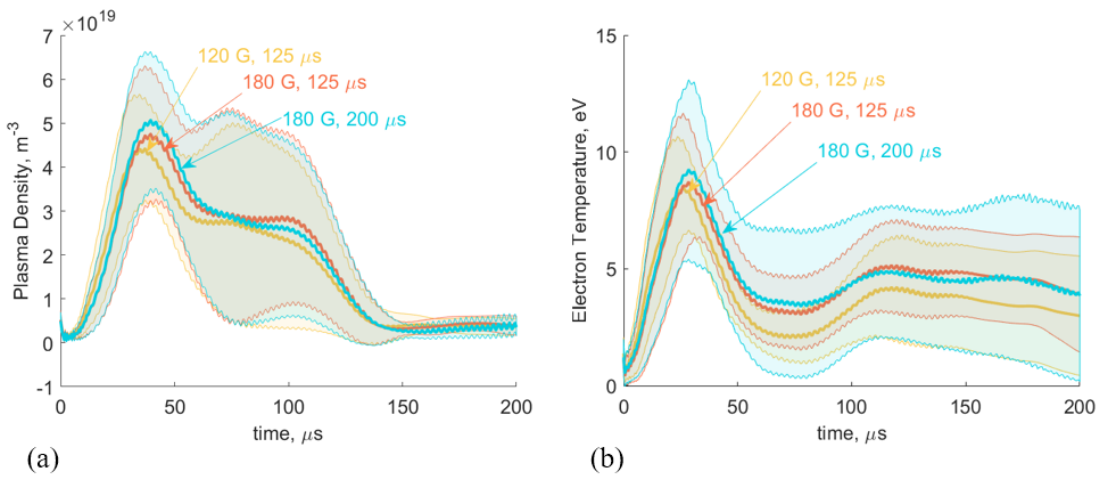


Fig. 10 Plots showing the a) plasma density and b) electron temperature for the 5.4 mg/s Xe flow rate conditions d-f in Table1

When we look at the differences between plots for magnetic field strength and pulse duration, we do not see a considerable change. This is partly due to the inaccuracies of the TLP, but is also an indication that these plasma parameters are relatively insensitive to these changes. Interestingly, we see that longer pulse lengths do not result in appreciably different conditions between 125 and 200 μs . However, we do know from our coupling measurements that these longer pulses do impart more energy to the plasma as can be seen in Fig. 12. It is possible that the longer pulse lengths allow for more magnetic energy storage in the plasma—which would not show up in our measurements here—or the extra energy is able to be coupled into surrounding structures while the plasma is present.

C. Evaluation of Energy Losses

We show in Fig. 11 the integrated power losses over time from Eqs. 14 and 11 for the six operating conditions we investigated for this study. We show in the filled areas the errors in these calculated powers assuming a standard 30% error in plasma density for a Langmuir probe. Similar to the spatially averaged values, we see a double peak form for both radiative and wall losses across conditions. For radiative losses, the peaks occur at roughly 40 μs and 100 μs after the start of RMF pulsing, and for wall losses these peaks occur near 30 μs and 80 μs . The cause of the wall losses occurring earlier in the pulse is the increased dependence on electron temperature which also peaks earlier.

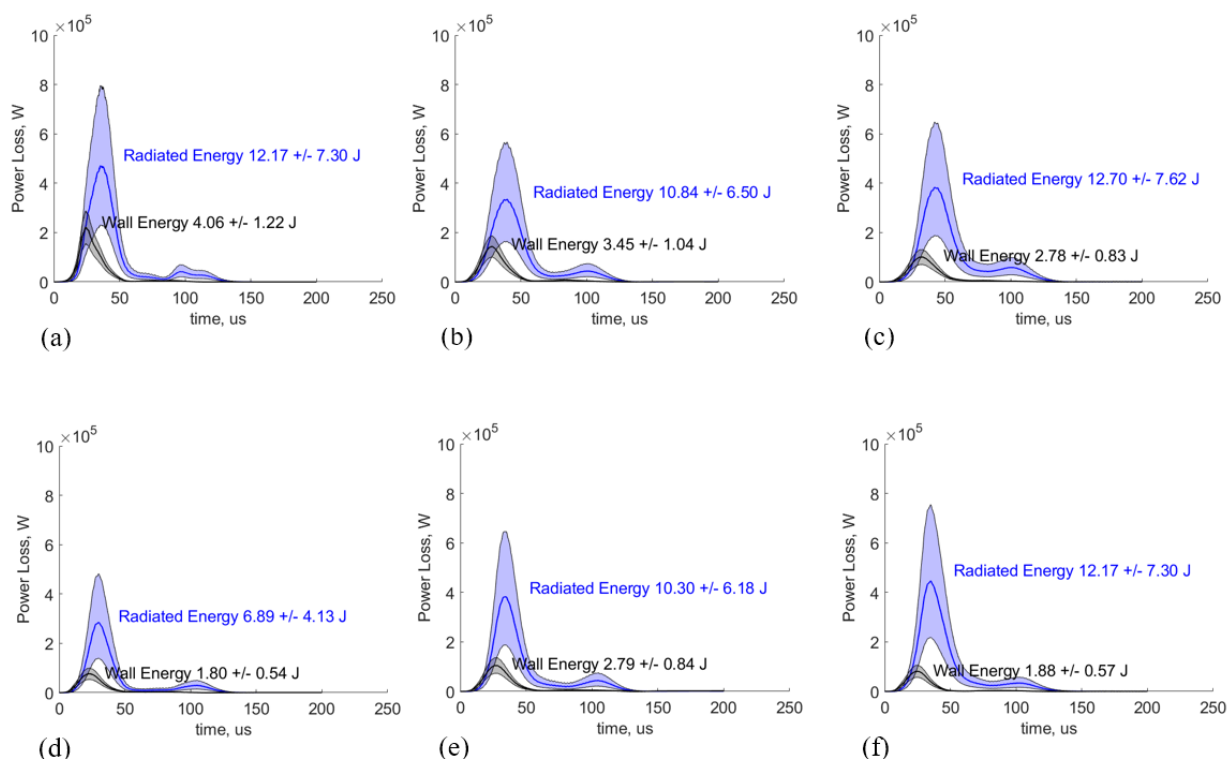


Fig. 11 Evaluated power losses in the thruster for operating conditions a-f from Table 1.

What becomes evident from these plots is that the radiative losses dominate over the wall losses, with radiation reaching typical peak powers of 300 kW, and wall losses reaching a typical peak power of 100 kW. This is contrary to our previous work [19], and is primarily due to the very high plasma densities we measure early in the pulse. Our previous techniques could only measure parameters immediately following the end of the RMF pulse, and we recorded a maximum density of $5 \times 10^{18} \text{ m}^{-3}$. Because of the quadratic density scaling, a factor of ten increase in density results in a factor of one hundred increase in the radiation losses.

In Fig. 12, we report the measured coupled plasma energy from Eq.10 as well as the time-integrated power losses from Fig. 11. We can see here that the sum of the two energy loss channels is greater than that of the coupled plasma energy for the 4.0 mg/s conditions, and the appropriate magnitude relative to the coupled energy for the 5.4 mg/s conditions. Given that the 4.0 mg/s cases are all over the total available energy, this suggests there may be a systematic

error in our experimental setup that is causing us to overpredict, specifically the plasma density. This error is likely caused by additional ram current into the probe due to the RMF environment, where the transverse magnetic field is driving increased electron flux to the probe beyond what is assumed by the TLP theory. However, for all cases the order of magnitude of our measurements is correct and within error (with the exception of condition 'a'). Therefore, they generally agree with our previous calculations of plasma efficiency that indicate 90% of the energy coupled to the plasma is lost. We address this effect further in our discussion of the TLP measurements in Sec. VI. However, since the calculations of the two loss mechanisms are based on the same data, we believe the relative contributions between wall and radiative losses is still valid. Given this, we turn in the next section to address potential changes to thruster design and operation to mitigate the combined loss from these two effects.

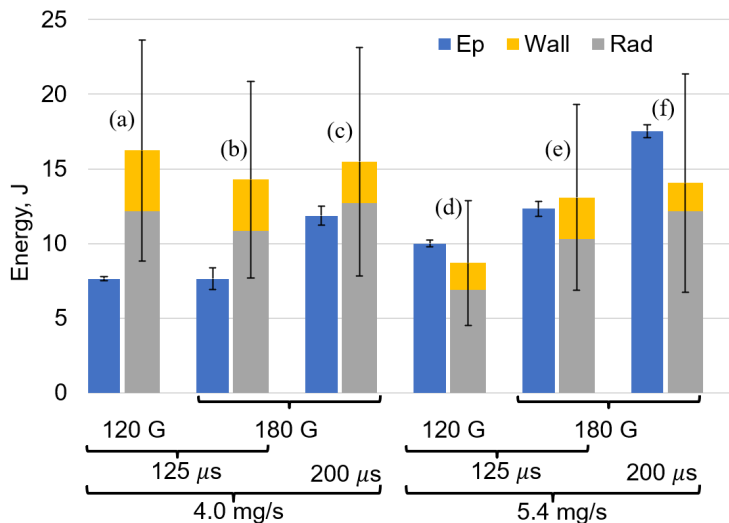


Fig. 12 Calculated coupled energy into plasma (E_p), integrated radiated energies (Rad), and integrated wall energies (Wall). Error bars on losses column indicate combined error for both mechanisms.

VI. Discussion

In this section, we begin with a discussion on the errors and caveats with the TLP measurement and methods to improve this experiment. Following this, we present several suggestions on how to improve RMF thruster performance given the results of this work.

A. TLP Measurement Considerations

We showed in the previous section that while the qualitative trends are consistent with data, we do overpredict the total energy for the lower flow rate conditions, and exceed our error bars for condition 'a'. We discuss in this section possible drivers for this. As mentioned previously, a probable cause for our systematic over prediction of plasma density is an unaccounted-for ram current. This could be a result of the RMF driving additional electrons into the probe which in theory would be more prominent at lower flow rates since there is less plasma density to screen out the RMF from the probe in these conditions.

Additionally, for the calculation of plasma density, we utilized OML theory based on the calculated ratios of probe radius to Debye length. This was chosen per the best practices developed by Lobbia et al. [27]. This single correction, while necessary, was over-constrained for the time-varying plasma we were attempting to measure, as the ratio of Debye length to probe radius varies significantly over time, particularly as the plasma cools and rarefies. One way this may be addressed is to increase our probe radius and reduce our bias voltage, V_{d3} , to enable a thin sheath approximation and to tune our bias closer to the electron temperature respectively.

B. Impacts to Thruster Design

From our results, it appears that a major driver for inefficiency is that our initial plasma densities are too high. This facilitates high radiation losses, which have previously been indicated as a major loss driver for RMF thrusters by Weber [15], and for the PIT thruster by Polzin [8]. For reference, the SPT-100 Hall thruster has a plasma density of roughly $1 \times 10^{17} \text{ m}^{-3}$ [21] which is two orders of magnitude less than the average densities in the RMF thruster. This means that the RMF is 10,000 times more radiative. This high ion density is largely in part due to the pulsed ionization scheme. From mass continuity, for a given mass flow rate, the density will be inversely proportional to particle velocity. This is written as:

$$n = \frac{\dot{m}}{m_i A v}, \quad (25)$$

where \dot{m} is the mass flow rate, m_i is the particle/ion mass, A is the cross sectional area, and v is the particle velocity. Quantitatively, for a mass flow rate of 4 mg/s, an area of 150 cm^2 , and a neutral velocity of 200 m/s, we would expect a neutral density of roughly $5 \times 10^{18} \text{ m}^{-3}$ which is close to our measured density. We do however inject most of our neutral gas upstream into the thruster which will further increase the density. In the RMF thruster, these slow neutrals are rapidly ionized by the RMF which leads to high ion densities, many excitation collisions, and large radiative losses. This ionization takes place on the order of tens of μs as shown by Figs. 9 and 10 which is much faster than their residence time, $t_{\text{residence}} = L/v_{\text{ex}}$, where v_{ex} is the effective exhaust velocity of the propellant. From direct performance measurements of specific impulse, residence times for the ions in the RMF thruster are greater than $100 \mu\text{s}$ [16], and therefore the ions have ample time to radiate energy. Because of this effect, we would like to employ methods to reduce these densities or the radiative power loss in general.

A simple geometric way to reduce the density while maintaining the mass bit per pulse would be to lengthen the thruster. Increasing the available volume for the neutral fill will allow a lower flow rate to achieve the same available propellant mass which directly reduces the density. If the thruster radius is unchanged, the coupling physics should be minimally effected, and the RMF antennas will have increased "contact" with the plasma slug. Another geometric solution is to implement a coaxial thruster configuration where the centerline flow is physically blocked. Any plasma that is formed along the thruster axis contributes to the radiative losses but contributes little to thrust because the stored magnetic energy we aim to drive scales like $E_b \propto en\omega r$, where ω is the RMF frequency, and r is the radial coordinate. Similar to the previous scheme, in this instance the total mass flow rate would be lowered to maintain the same density in the annular region, but the plasma density that previously existed on centerline would be eliminated. However for both of these schemes, there is a trade-off as they both increase the wall area, and therefore will increase the wall losses. Although, because the wall losses will increase linearly with area and the radiative losses will decrease quadratically with density, there is likely an optimum configuration to minimize both these loss modes where their magnitudes are equal.

Additionally, RMF thruster performance could be improved through operational changes. The method that has been suggested by other authors [8, 15] is to switch to alternative propellants. Typically we use xenon gas in electric propulsion devices due to its low ionization energy and large cross-section. However, given that the RMF does not suffer from low mass utilization and is a prolific ionizer, a propellant such as argon, nitrogen, or molecular compounds such as CO_2 or ammonia may be better choices. In fact, the PIT mk.V thruster was able to achieve its highest efficiency on ammonia with minimal radiative losses as the explanation [8]. The plausible reasoning behind this is for these other propellants excitation and ionization collisions occur at a reduced rate and the molecules will instead absorb energy into rotational and vibrations modes which are less of a detriment to performance. Alternatively, another scheme for reducing the radiative losses is to operate the thruster in a constant wave (CW) mode where the RMF is continuously operating. The advantage of this is that as the neutrals enter the thruster they will be quickly ionized and ejected and the average particle speed will remain high and the densities low. This continuous operation is why Hall thrusters of similar sizes can operate at much higher flow rates without incurring radiative loss problems. Arguably, the Hall thruster also does most of its ionization when the gas is still moving slowly. However, this ionization region is relatively thin as the ions immediately start to accelerate thus reducing the density over the bulk of the internal thruster volume. This is the type of structure we would like to achieve in a CW RMF thruster. The limitation of this method is the power processing. To maintain our ionization we require kA level currents through the RMF antennas, which is not achievable at steady state for our 5 kW-class thruster. To address this, we could utilize pulse shaping techniques in which a large current pulse initiates ionization and then is slowly ramped down to a background level that can maintain the discharge at a reduced amplitude. Hugrass and Jones numerically investigated this operation for a steady RMF ionization source and found it is theoretically possible [28].

VII. Conclusion

In this work we sought to investigate the previously measured low plasma efficiencies found for RMF thrusters, where a small (roughly 10%) fraction of the coupled RMF energy is stored as useful magnetic energy in the azimuthal electron current. We evaluated two energy loss channels: radiative losses due to excitation collisions, and wall losses due to thermal electron diffusion to the floating thruster walls by employing a triple Langmuir probe to make instantaneous measurements of the plasma density and electron temperature over the internal volume of the thruster. We found that radiative losses are the dominant loss mechanism, as on average they constitute 80% of the total losses. This was true for the six thruster operating conditions we investigated, where we varied the mass flow rate, bias magnetic field strength, and RMF pulse length. These radiative losses are the result of high ion densities that occur early in the RMF pulse and achieve values of up to $5 \times 10^{19} \text{ m}^{-3}$. Furthermore, we proposed several techniques to mitigate these losses, including varying thruster geometry, switching to alternative propellants, and operating the thruster in a continuous manner. In summary, now that the root cause of poor RMF thruster efficiency in our system has been identified, there are potential paths to evaluate for future thruster designs as we seek to assuage these losses.

Acknowledgements

We would like to thank Eagle Harbor Technologies for their development of the RMF power processing unit and their technical support. Furthermore, we would like acknowledge the sponsors of this work. Funding was supplied under an Air Force SBIR grant, NSTGRO Fellowship grant Number 80NSSC20K1168, and NSTRF Fellowship grant number 80NSSC18K1190.

References

- [1] Polzin, K. A., “Scaling and systems considerations in pulsed inductive plasma thrusters,” *IEEE Transactions on Plasma Science*, Vol. 36, 2008, pp. 2189–2198. <https://doi.org/10.1109/TPS.2008.2003537>.
- [2] Polzin, K. A., Martin, A. K., Little, J., Promislow, C., Jorns, B. A., and Woods, J. M., “State-of-the-art and advancement paths for inductive pulsed plasma thrusters,” *Aerospace*, Vol. 7, 2020, pp. 1–67. <https://doi.org/10.3390/AEROSPACE7080105>, URL <https://www.mdpi.com/2226-4310/7/8/105>.
- [3] Polzin, K. A., Martin, A. K., Eskridge, R. H., Kimberlin, A. C., Addona, B. M., Devineni, A. P., Dugal-Whitehead, N. R., and Hallock, A. K., “Summary of the 2012 Inductive Pulsed Plasma Thruster Development and Testing Program,” 2013. URL <https://ntrs.nasa.gov/api/citations/20140002426/downloads/20140002426.pdf>.
- [4] Mikellides, P. G., “Pulsed Inductive Thruster (PIT): Modeling and Validation Using the MACH2 Code,” 2003, pp. 1–8. URL <http://hdl.handle.net/2060/20040027584>.
- [5] Kirtley, D. E., Slough, J. T., Pfaff, M., and Pihl, C., “Steady Operation of an Electromagnetic Plasmoid Thruster,” 2011, pp. 1–18.
- [6] Waldock, J., Kirtley, D. E., and Slough, J. T., “Electromagnetic Optimization of FRC-Based Pulsed Plasma Thrusters,” 2013, pp. 1–14.
- [7] Mikellides, P. G., and Villarreal, J. K., “High energy pulsed inductive thruster modeling operating with ammonia propellant,” *Journal of Applied Physics*, Vol. 102, 2007, pp. 1–12. <https://doi.org/10.1063/1.2809436>.
- [8] Polzin, K. A., “Comprehensive review of planar pulsed inductive plasma thruster research and technology,” *Journal of Propulsion and Power*, Vol. 27, 2011, pp. 513–531. <https://doi.org/10.2514/1.B34188>, URL <http://arc.aiaa.org/doi/10.2514/1.B34188>.
- [9] Slough, J. T., Kirtley, D. E., and Weber, T. E., “Pulsed Plasmoid Propulsion: The ELF Thruster,” 2009, pp. 1–24. URL https://s3-us-west-2.amazonaws.com/pnwmsnw/ELF_IEPC-2009-265.pdf.
- [10] Weber, T. E., Slough, J. T., and Kirtley, D. E., “The electrodeless Lorentz force (ELF) thruster experimental facility,” *Review of Scientific Instruments*, Vol. 83, 2012, pp. 83,113509. <https://doi.org/10.1063/1.4759000>.
- [11] Furukawa, T., Shimura, K., Kuwahara, D., and Shinohara, S., “Verification of azimuthal current generation employing a rotating magnetic field plasma acceleration method in an open magnetic field configuration,” *Physics of Plasmas*, Vol. 26, 2019. <https://doi.org/10.1063/1.5064392>, URL <http://dx.doi.org/10.1063/1.5064392>.

- [12] Furukawa, T., Shinohara, S., and Kuwahara, D., “Electrodeless plasma propulsion with electromagnetic acceleration effect by using rotating magnetic field current drive method,” *AIAA Propulsion and Energy 2020 Forum*, 2020, pp. 1–11. <https://doi.org/10.2514/6.2020-3630>.
- [13] Woods, J. M., Sercel, C. L., Gill, T. M., and Jorns, B. A., “Performance measurements of a rotating magnetic field thruster,” *AIAA Propulsion and Energy 2020 Forum*, Vol. 3633, 2020, pp. 1–18. <https://doi.org/10.2514/6.2020-3633>.
- [14] Sercel, C. L., Woods, J. M., Gill, T. M., and Jorns, B. A., “Impact of flux conservers on performance of inductively driven pulsed plasmoid thrusters,” *AIAA Propulsion and Energy 2020 Forum*, 2020, pp. 1–17. <https://doi.org/10.2514/6.2020-3632>.
- [15] Weber, T., “The Electrodeless Lorentz Force Thruster Experiment,” 2010. URL <https://digital.lib.washington.edu/researchworks/handle/1773/20069>.
- [16] Sercel, C. L., Gill, T., Woods, J. M., and Jorns, B., “Performance Measurements of a 5 kW-Class Rotating Magnetic Field Thruster,” American Institute of Aeronautics and Astronautics, 2021, pp. 1–26. <https://doi.org/10.2514/6.2021-3384>, URL <https://arc.aiaa.org/doi/10.2514/6.2021-3384>.
- [17] Brackbill, J., Cambier, J. L., Gimelshein, N. E., and Gimelshein, S. F., “Numerical analysis of neutral entrainment effect on field-reversed configuration thruster efficiency,” *Journal of Propulsion and Power*, Vol. 30, 2014, pp. 1450–1458. <https://doi.org/10.2514/1.B35260>.
- [18] Koo, J., Sousa, E. M., and Martin, R., “High Fidelity Modeling of Field-Reversed Configuration (FRC) Thrusters,” 2017.
- [19] Gill, T., Sercel, C. L., Woods, J. M., and Jorns, B. A., “Experimental Characterization of Efficiency Modes in a Rotating Magnetic Field Thruster,” American Institute of Aeronautics and Astronautics (AIAA), 2022. <https://doi.org/10.2514/6.2022-2191>.
- [20] Hugrass, W. N., “Cylindrical Plasma Equilibria Maintained by Means of a Rotating Magnetic Field,” *Journal of Plasma Physics*, Vol. 28, 1982, pp. 369–378. <https://doi.org/10.1017/S0022377800000337>.
- [21] Goebel, D. M., and Katz, I., *Fundamentals of Electric Propulsion: Ion and Hall Thrusters*, Jet Propulsion Laboratory, California Institute of Technology, 2008. <https://doi.org/10.1002/9780470436448>.
- [22] Mikellides, L. G., Katz, I., Mandell, M., and Snyder, J. S., “A 1-d model of the hall-effect thruster with an exhaust region,” American Institute of Aeronautics and Astronautics Inc., 2001. <https://doi.org/10.2514/6.2001-3505>.
- [23] Hayashi, M., “Luminous layers in the prebreakdown region of low pressure noble gases,” *J. Phys. D: Appl. Phys.*, Vol. 15, 1982, pp. 1411–1418.
- [24] Hayashi, M., “Determination of electron-xenon total excitation cross-sections, from threshold to 100 eV, from experimental values of Townsend’s alpha,” *J. Phys. D: Appl. Phys.*, Vol. 16, 1983, pp. 581–589.
- [25] Miller, K. E., Prager, J., Henson, A., McEleney, K., Woods, J., Sercel, C., Gill, T., Viges, E., and Jorns, B., “Continuously-Operating Repetitively-Pulsed RMF-FRC Thruster and Power System,” IEEE, 2021, pp. 1–1. <https://doi.org/10.1109/ICOPS36761.2021.9588361>.
- [26] Chen, S. L., and Sekiguchi, T., “Instantaneous direct-display system of plasma parameters by means of triple probe,” *Journal of Applied Physics*, Vol. 36, 1965, pp. 2363–2375. <https://doi.org/10.1063/1.1714492>.
- [27] Lobbia, R. B., and Beal, B. E., “Recommended practice for use of langmuir probes in electric propulsion testing,” *Journal of Propulsion and Power*, Vol. 33, 2017, pp. 566–581. <https://doi.org/10.2514/1.B35531>.
- [28] Hugrass, W. N., “Existence of Non-Unique Steady State Solutions To the Rmf Current Drive Equations.” *Australian Journal of Physics*, Vol. 38, 1985, pp. 157–169. <https://doi.org/10.1071/PH850157>.